

An Experimental Investigation of Wideband MIMO Channel Characteristics Based on Outdoor Non-LOS Measurements at 1.8 GHz

Yaoqing Yang, *Member, IEEE*, Guanghan Xu, *Member, IEEE*, and Hao Ling, *Fellow, IEEE*

Abstract—This paper presents an experimental investigation of the wideband MIMO channel characteristics in an outdoor non-line-of-sight environment. Our wideband MIMO testbed is a true array system with four transmitting antennas and eight receiving antennas, which operates at a carrier frequency of 1.8 GHz with a bandwidth of 2.5 MHz. The measurements are conducted at the J. J. Pickle Research Campus at the University of Texas at Austin. From the measured data, the matrix channel complex impulse responses and multipath delay profiles are extracted. Statistical descriptions of the elements in the channel matrices and the frequency correlation functions are also presented. Based on the measured data, the channel capacities are computed and the Kronecker model results are evaluated for arrays of different sizes. It shows that the Kronecker model underestimates the channel capacities due to higher correlation matrices for arrays of larger sizes in outdoor environments.

Index Terms—Channel capacity, channel impulse response, multipath delay profile, wideband multiple-input-multiple-output (MIMO) channel.

I. INTRODUCTION

THE demand for capacity in wireless communications has given rise to much research on multiple transmitter (Tx) and multiple receiver (Rx) antenna systems. In rich scattering environments, narrowband multiple-input-multiple-output (MIMO) systems can significantly increase the channel capacity over that of traditional single antenna systems [1], [2]. In contrast with conventional smart antennas, which improve the quality of the transmission of a single data stream, MIMO systems have the potential to provide multiple independent transmission channels. MIMO schemes have been introduced in the IEEE 802.11n and 802.15 standards for high throughput, wireless local-area and personal-area networks. Realistic MIMO channels, however, exhibit some degree of correlation among the multiple transmitting antennas and receiving

antennas. Consequently, the achievable capacity in practice may be lower than that of theoretical expectations [3]. More recently, researchers have investigated the performance of frequency-selective, or wideband, MIMO channels [4]–[8].

Measurements provide the most direct way to evaluate MIMO channels. Different approaches have been reported on measuring MIMO channel features. For example, Chizhik *et al.* conducted a capacity study in Manhattan by using a 16 Tx and 16 Rx narrowband channel sounder with a bandwidth of 32 kHz [9]. Wallace *et al.* conducted narrowband indoor MIMO measurements at 2.45 GHz at the Brigham Young University campus [10]. This is a true array system, where all antennas operate simultaneously, and such a system most closely models real-world MIMO communication [11]. A 2 Tx by 2 Rx wideband MIMO channel system [12], based on the orthogonal frequency division multiplexing (OFDM) technique consisting of 751 subcarriers spaced 25 kHz apart, was used to measure the wideband channel impulse response in suburban Chicago. The Medav RUSK channel sounders were used to take measurements at the University of Bristol, U.K. [5] as well as other sites [6], [13]. This virtual array system connects an antenna array to a single receiver via a fast radio frequency (RF) switch. It operates at 5.2 GHz with a bandwidth of up to 120 MHz. Another virtual wideband MIMO system employing fast switches at Rx side was used to conduct measurements of indoor 16×32 wideband MIMO channel at 5.8 GHz with a bandwidth of 100 MHz [14], [15]. MIMO channel characteristics were also investigated over small handheld terminals [16], [17]. A series of fixed wireless 2×2 MIMO channel measurements and modeling were conducted at 2.5 GHz [18]–[20].

In this paper, we report on a 4×8 true array channel sounder for characterizing wideband MIMO channels. The sounder operates at a carrier frequency of 1.8 GHz with a bandwidth of 2.5 MHz. Wideband MIMO channel measurements pose a challenge because of the higher requirement for multiple channel data acquisition. Our system uses the spread spectrum technique to simultaneously transmit multiple pseudorandom signals. Multiple receivers then receive the transmitted signals simultaneously. Consequently, the system can more faithfully capture the wideband MIMO channel features in the real environment. Furthermore, it has separate Tx and Rx systems to allow for long range outdoor testing without the need for cable connections. A series of field measurements under nonline-of-sight (NLOS) scenarios is conducted using the wideband channel sounder at the J. J. Pickle Research Campus at the University of Texas at Austin. From the raw

Manuscript received September 13, 2005; revised May 15, 2006. This work was supported in part by the Texas Higher Education Coordinating Board under the Texas Advanced Technology Program, by a research grant from The University of Texas at Austin, and in part by the National Science Foundation Major Research Instrumentation Program.

Y. Yang was with the Department of Electrical and Computer Engineering, The University of Texas at Austin, Austin, TX 78712 USA. He is now with the Department of Computer and Electronics Engineering, University of Nebraska-Lincoln (Omaha Campus), Omaha, NE 68182 USA.

G. Xu is with the Beijing Xinwei Telecom Technology, Inc., Beijing, China.

H. Ling is with the Department of Electrical and Computer Engineering, The University of Texas at Austin, Austin, TX 78712 USA.

Color versions of Figs. 2, 3, 5–11 available online at <http://ieeexplore.ieee.org>.

Digital Object Identifier 10.1109/TAP.2006.883960

data, the complex impulse responses are extracted based on the cross-correlation properties between the received signals and the probing pseudorandom noise (PN) sequence. Statistical descriptions of the elements in the channel matrices and the frequency correlation function are presented. The measured channel capacities are then calculated and compared with those based on the Kronecker model [5], [21].

The paper is organized as follows. In Section II, we describe the architecture of our wideband MIMO channel sounder. Section III describes the measurement scenarios and channel data collection under NLOS environments. The channel feature extraction process and the characteristics of the measured channels, including multipath delay profiles, rms delay spread and frequency correlation functions, are described in Section IV. In Section V, we present the measured MIMO channel capacity. Based on the measured subarray data, the Kronecker MIMO channel model is evaluated by comparing the cumulative density function (CDF) of the capacity derived from the measured channels, the independent identically distributed (iid) simulation, and the Kronecker model. Finally, Section VI presents our concluding remarks.

II. DESIGN AND IMPLEMENTATION OF WIDEBAND MIMO CHANNEL SOUNDER

Our wideband MIMO channel sounder consists of three parts: the transmitter testbed, the receiver testbed, and the multiple antenna arrays.

A. Transmitter

The Tx testbed consists of four identical transmitting modules, a local oscillator (LO) synthesizer, and a field-programmable gate array (FPGA) board. Each Tx module transmits a probing PN sequence with good autocorrelation properties. This probing sequence is a complex PN sequence with only one significant peak in its autocorrelation. Three additional PN sequences are generated by shifting the original probing PN sequences by a quarter of its length. The four PN sequences are then used as the four Tx signals. In this system, the sequences of the in-phase (I) and quadrature (Q) branch are composed of 120 data points, respectively. Thirty prefix data points and thirty postfix data points are added at both the beginning and the end of the data sequences to facilitate the postprocessing of the received data. Four times oversampling is imposed on the Tx data sequences. Thus, a sequence of $(30 + 120 + 30) \times 4 = 720$ points is obtained. Afterwards, a 33-point raised cosine pulse-shaping filter is applied to the Tx data sequences. Consequently, the length of the PN data sequence amounts to 752 points, which is designed to fit in the memory of the FPGA. Four sets of I and Q data sequences are output synchronously from the FPGA to four dual-channel digital-to-analog converters (Analog Device AD9761) with a chip frequency of 10 MHz. Antialiasing filters are used to remove frequency components higher than 2.5 MHz in the Tx baseband signals.

Fig. 1(a) shows the block diagram of the Tx testbed. The four filtered baseband signals are modulated with an intermediate-frequency (IF) LO of 138.625 MHz. They are then upconverted to an RF of 1.8 GHz. Very-stable LO signals are syn-

thesized by a phase lock loop (PLL) board. The RF signals are amplified up to 27 dBm at the front ends of the Tx antennas. Due to losses from the coaxial cables and component discrepancies among the Tx modules, the power levels of the four RF signals are not exactly the same in practice. Therefore, we have to remove these differences by calibration. The calibration procedure entails bypassing the antennas by using a cable (and an attenuator) to connect a Tx front-end and the Rx1 front-end with all the other transmitters and receivers terminated. By transmitting the probing sequence, we can determine the peak correlation value for this Tx-Rx1 pair. This process is repeated for all four transmitters. The four peak correlation values are then stored as calibration coefficients for postprocessing.

B. Receiver

The Rx testbed consists of eight identical receiving modules, an LO synthesizer, four data acquisition cards, and an FPGA control unit. In Fig. 1(b), the Rx LOs are generated by the PLL in the same way as for the Tx testbed. All signals from the Rx antennas are first downconverted to IF signals. They then go through the mixers to be demodulated into eight I and Q baseband signals. All baseband signals are sampled simultaneously at the rate of 10 MHz and digitized at 12-bit resolution by the National Instrument data acquisition cards (DAQ)-(PCI-6115). Four DAQ cards in the computer collect the channel data onto the hard drive for postprocessing. The maximum number of samples for a snapshot is 200 000. This corresponds to 20 ms of data at a sampling rate of 10 MHz, and is limited by the DAQ on-board memory. Rx calibration has to be performed because of the gain differences and cable losses among the eight Rx modules. The Rx calibration procedure is similar to the Tx calibration. We choose Tx1 as a reference transmitter and find the peak correlation values for all eight receivers. They are also stored as calibration coefficients for postprocessing.

Another important issue is the carrier frequency offset estimation. Frequency mismatch between the transmitter and receiver LOs can occur. The carrier frequency of a few GHz typically has offsets of up to a few kHz. The offset can be estimated through the phase variation of the received signals after despreading. The estimated frequency offset is assumed to be static and used to compensate the received signal via a numerically controlled oscillator during the postprocessing. Fig. 2 shows a picture of (left) the Tx testbed and (right) the Rx testbed.

C. Antenna Arrays

The transmitter is a uniform linear array (ULA) consisting of four antenna elements. The element spacing of the Tx array is fixed at 1λ , where $\lambda = 16.7$ cm is the radio wavelength. The Tx antennas are quarter-wave monopoles. The receivers use a ULA with eight antennas. The element spacing of the Rx array is adjusted to either 0.5λ or 1λ for different measurement setups. The Rx antennas are colinear dipoles. The Rx testbed is carried inside a van, and the Rx antenna array is mounted on a wooden supporting stand.

The wideband channel sounder is designed to achieve a maximum excess delay of 12 μ s and a minimum resolvable delay of 0.4 μ s. The maximum delay that can be measured is determined by the 120 data points of the PN probing sequences and the chip

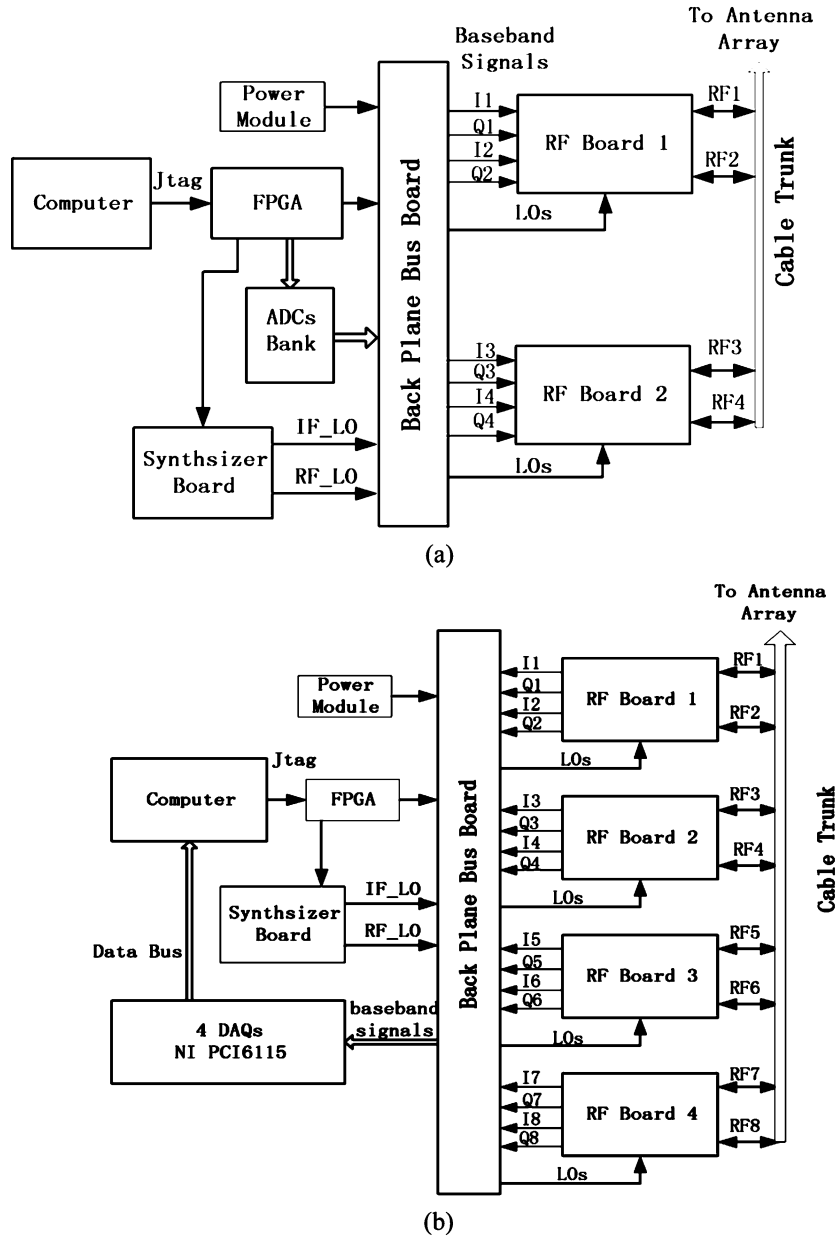


Fig. 1. Block diagram of Tx module and Rx module. (a) Block diagram of transmitters. (b) Block diagram of receivers.

rate of 10 MHz. The minimum resolvable delay results from the sampling rate of 10 MHz and four times oversampling. As a result, the bandwidth of the baseband signals is 2.5 MHz, which is equivalent to a delay resolution of $0.4 \mu\text{s}$.

III. MEASUREMENT ENVIRONMENTS AND DATA COLLECTION

A. Descriptions of Measurement Scenarios

Fig. 3 shows the partial layout of the measurement site at the J. J. Pickle Research Campus of the University of Texas at Austin, which includes about 50 buildings. All of the buildings are either one or two stories high, and they are labeled by numbers. In this paper, the Tx antenna array is located at TX_Loc on the roof of Building 16, which is 6 m high. The Rx antenna array stands 60 cm above the ground with a wooden supporting stand west of

Building MER 160, where the sites of RX_Loc1 and RX_Loc2 are located for the field measurements.

Since Building MER 160 is a comparatively tall building at 25 m in height, it completely blocks the direct path from Tx to Rx. The distance between TX_Loc and RX_Loc1 is approximately 200 m without the blockage caused by MER 160, and the distance between TX_Loc and RX_Loc2 is approximately 350 m. Other buildings within this area as well as a row of buildings to the south of the site (not shown in the figure) contribute to the reflective radio paths. Thus, this is a typical obstructed line of sight or NLOS suburban scenario.

B. Channel Data Collection

To study the wideband MIMO channel features, we conduct a series of measurements according to the antenna array locations and Rx interelement spacing as follows. The position of the Tx



Fig. 2. Picture of (left) transmitters and (right) receivers inside van.

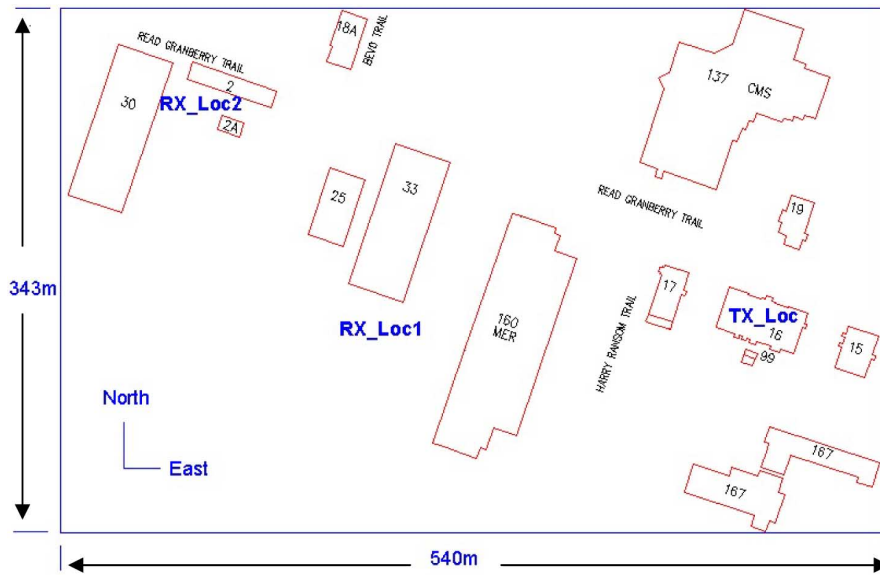


Fig. 3. Layout of measurement scenarios.

antenna array is fixed on the roof of Building 16, but the position of the Rx antenna array on the ground is moved over a distance of 10λ at the site of RX_Loc1 or RX_Loc2. The Rx gains are selected such that the received baseband signals are not too strong to cause saturation (3 V peak-to-peak) while maintaining sufficient signal-to-noise ratio (SNR). Then, we fix the gain values during the measurements.

Fig. 4 shows the procedure for the data collection. First, the Rx antenna array with interelement spacing $\Delta_1 = 0.5\lambda$ is set at the site of RX_Loc1. The initial position of the Rx array is selected arbitrarily. The Rx antenna array is then moved by steps of 0.1λ . For the sake of reliability, three snapshots are taken while the Rx array remains at the same position. One snapshot

is configured to collect 10 000 samples of Rx data at the 10 MHz sampling rate. We choose 12 of the $(10\,000 \div 752) \cong 13$ periods for data analysis. Therefore, there is a total of $12 \times 3 = 36$ repeated measurements per Rx position, and a total of $36 \times 101 = 3\,636$ channel matrix realizations from the 101 positions. Next, the Rx antenna interelement spacing is adjusted to 1λ , and we rerun all of the measurements using the same procedure as that for $\Delta_1 = 0.5\lambda$. Finally, the Rx testbed is moved to the site of RX_Loc2, and we repeat all of the measurement procedures as at RX_Loc1. In all, we collect $3\,636 \times 2 \times 2 = 14\,544$ matrix channel realizations, which are associated with the Rx array locations, interelement spacing of the Rx array, and NLOS environments.

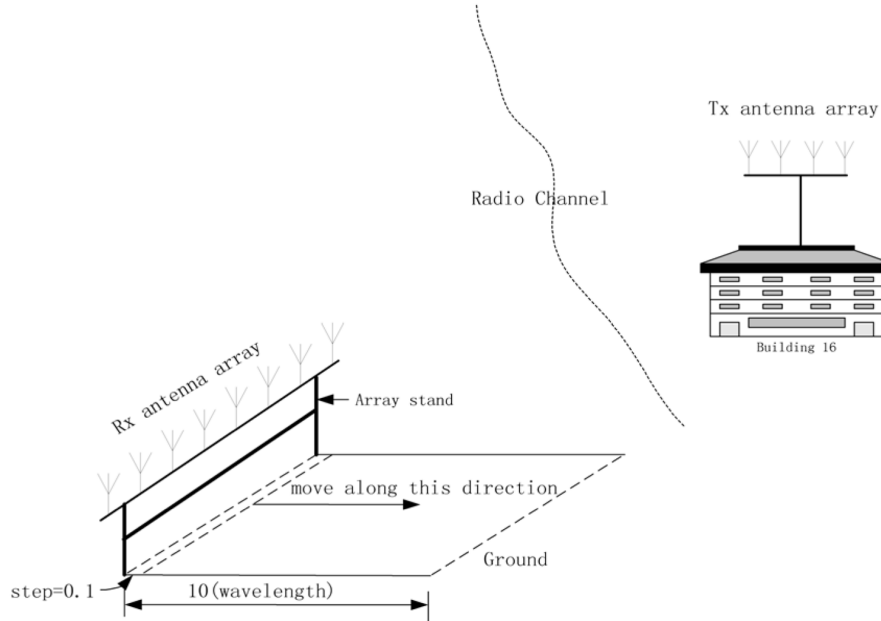


Fig. 4. Measurement snapshots versus Rx array locations.

IV. CHARACTERISTICS OF MEASURED WIDEBAND CHANNELS

In this section, we first extract the matrix channel impulse responses from the measured data, and then present the basic characteristics of the wideband MIMO channels including rms delay spreads, statistics of the channel matrix elements and frequency correlation functions.

A. Extraction of Channel Impulse Responses

A general time- and frequency-selective MIMO radio channel can be described by the channel matrix $\mathbf{H}(\tau, t)$, which depends on the delay τ and the time instant t [22]. An alternative representation in the frequency domain can be obtained by applying the Fourier transform with respect to the delay τ .

Consider the case in which only one receiver receives the four transmitted signals and their replicas from the multipaths. Assume that the carrier frequency offset is compensated and the received sequences are synchronized with the probing PN sequence. Notice that there is multiple access interference in this case because of the correlation between the four transmitted signals. Given the four channel responses $h_1(l), h_2(l), h_3(l)$, and $h_4(l)$, and the four probing signals $s_1(n), s_2(n), s_3(n)$, and $s_4(n)$ in discrete time form, where n is the index of the transmitted sequence and l is the index of the multipath component, the received signal $d(n)$ can be expressed as

$$d(n) = \sum_{j=1}^{M_T} \sum_{l=0}^{L-1} h_j(l) s_j(n-l) + \eta(n) \quad (1)$$

where j is the transmitter number, M_T is the number of Tx antennas, L is the number of resolvable multipath components, and $\eta(n)$ is additive white Gaussian noise. Now we correlate the received signal $d(n)$ in (1) with $s_1(n)$, the probing PN sequence of Tx1. Because the transmitted signals are designed by circularly shifting the probing sequence one-quarter length of the pe-

riod, we obtain four correlation components equally spaced over the period of the PN sequence. The time span between adjacent correlation components is $12 \mu\text{s}$ in this channel sounder. Since we are using circularly shifted PN sequences, there is little multiple access interference in our testbed. Similarly, each of the eight received signals is extracted in the same way as the above channel impulse response extraction, and a total of 32 channel impulse responses are obtained.

Fig. 5 shows an example of the MIMO multipath delay profiles of a snapshot between four transmitters and eight receivers. Because a Tx to Rx link is modeled as a tapped-delay line, we can acquire $4 \times 8 = 32$ pairs of channel responses simultaneously. In order to align the recorded channel impulse responses in time, we search for the starting point of the first period of probing sequence from the raw data in one snapshot, and then align the recorded channel impulse responses in time. The channel length is 30 taps or $12 \mu\text{s}$ long, and 12 multipath delay profiles in a snapshot are superimposed on top of each other. The curves overlap and are nearly indistinguishable. Thus, the channel is quite stable within a snapshot. It is observed that two or three resolvable multipath components exist in these profiles.

B. Power Delay Profiles

In wideband channels, the averaged power delay profile (PDP) of a channel is found by taking the spatial average of the multipath delay profiles over a small area [23]. By making several local area measurements in different locations, it is possible to build an ensemble of power delay profiles. In the measurements, each snapshot contains $12 \times 32 = 432$ multipath delay profiles.

Fig. 6 shows an example of the averaged power delay profile that is calculated from one snapshot when Rx is located at RX_Loc1. Note that the calibration coefficients have been applied and the threshold of the PDP is set to 18 dB. There are two noticeable multipaths at 1.5 and $3.4 \mu\text{s}$, respectively.

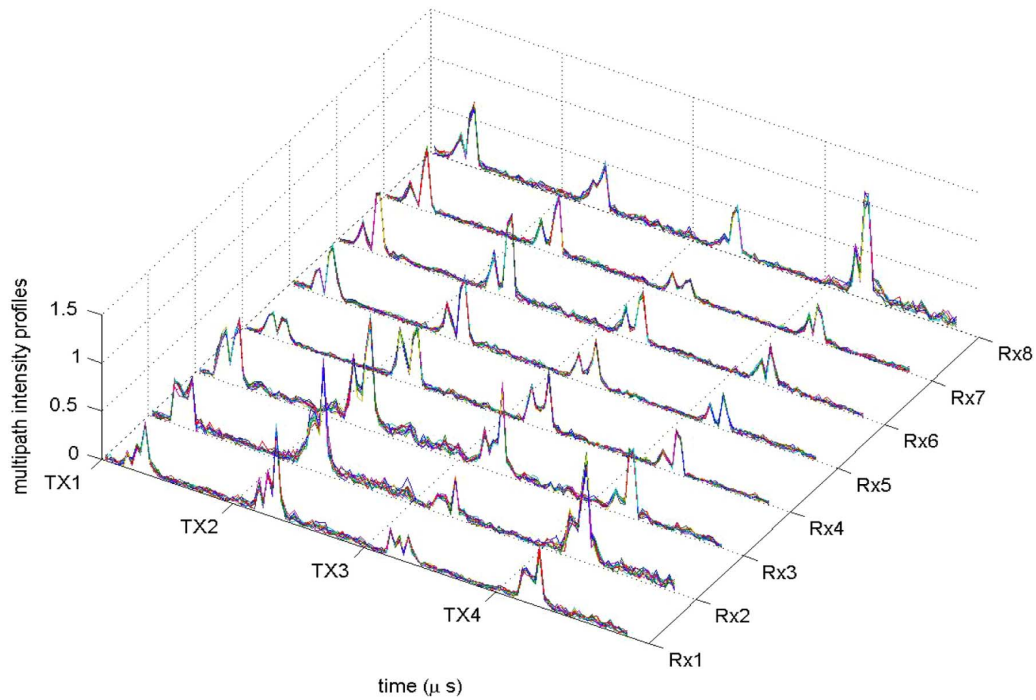


Fig. 5. An example of multipath intensity profiles by a snapshot.

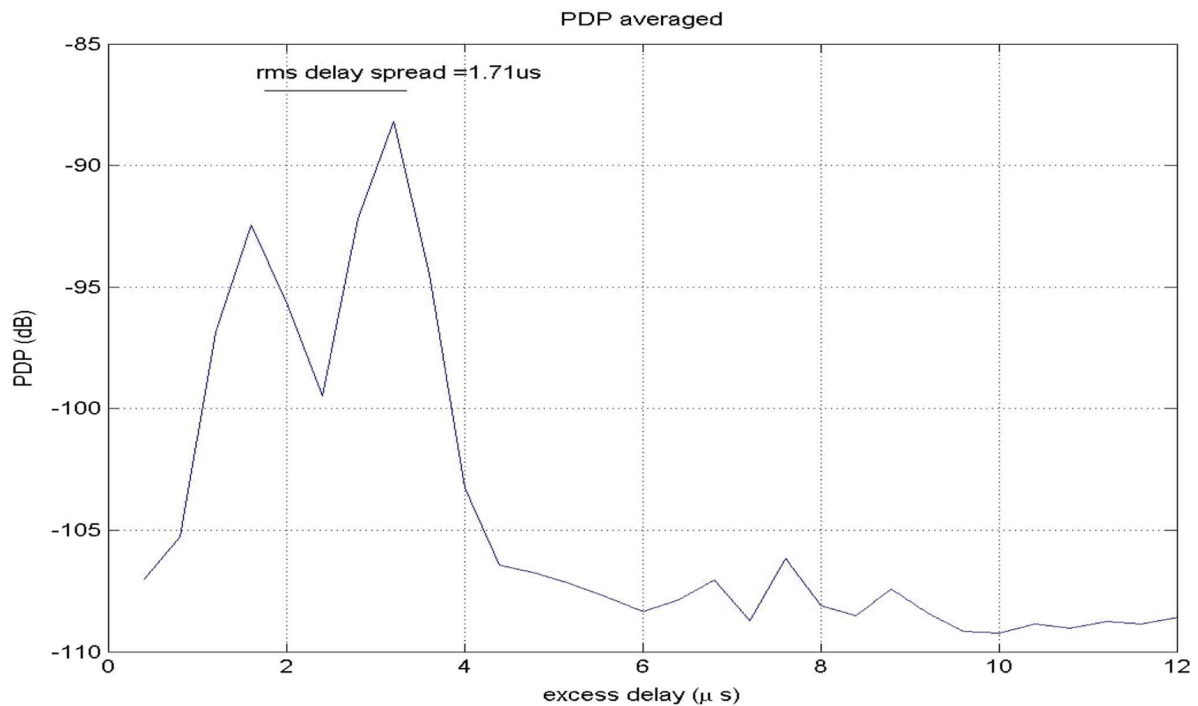


Fig. 6. Averaged power delay profile.

The rms delay spread is a good measure of the channel dispersion. It is defined as the square root of the second central moment of power delay profile [24]. The measurement result shows an rms delay spread of $\tau_{\text{rms}} = 1.58 \mu\text{s}$ at RX_Loc1 and $\tau_{\text{rms}} = 1.42 \mu\text{s}$ at RX_Loc2. If the coherence bandwidth B_c is defined as the bandwidth over which the frequency correlation function

is above 0.9 [23], then $B_c \approx 1/(50\tau_{\text{rms}}) = 12.658 \text{ kHz}$ and 14.085 kHz at RX_Loc1 and RX_Loc2, respectively. This ballpark estimate shows that the spectrum of the transmitted signals (2.5 MHz) has much wider bandwidth than the coherence bandwidth of the channel. Therefore, the measurement environments are well classified as frequency-selective (wideband).

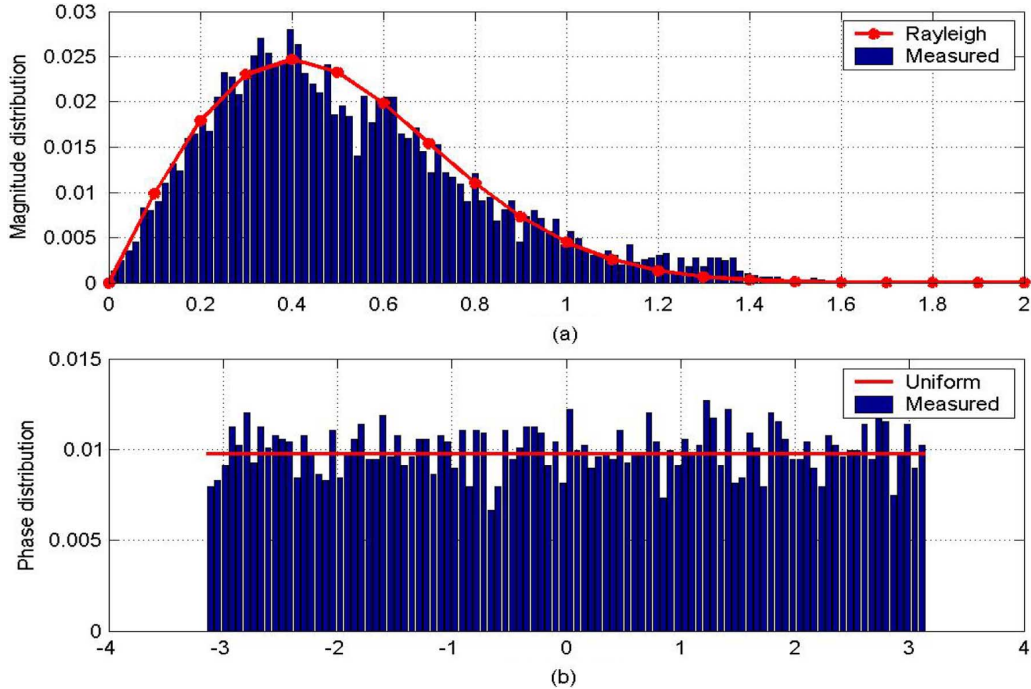


Fig. 7. Histograms of matrix channel response in a frequency bin. (a) Magnitude $|H|$. (b) Phase. Angle (H).

C. Statistics of the Channel Matrix Elements

After collecting all of the channel data, it is necessary to study the marginal PDF for the magnitude and phase of the elements of the MIMO channel matrix. Matrix channel frequency responses can be obtained by using the FFT over all channel impulse responses. Because the complex channel impulse responses are aligned in time, the phase information is preserved after the FFT manipulation. Since the maximum channel bandwidth of the channel sounder is 2.5 MHz, we can split the bandwidth into $\Omega = 128$ frequency bins. Thus, the bandwidth of the frequency bin is 19.531 kHz. The histograms of the magnitude and phase are defined as follows [10]:

$$p_{\text{mag}}[x] = \frac{1}{KM_T M_R \delta x} \underbrace{\text{HIST}}_{K, M_T, M_R} \left(\text{abs} \left(H_{mn}^{(k)} \right), \delta x \right) \quad (2)$$

$$p_{\text{pha}}[x] = \frac{1}{KM_T M_R \delta x} \underbrace{\text{HIST}}_{K, M_T, M_R} \left(\text{angle} \left(H_{mn}^{(k)} \right), \delta x \right) \quad (3)$$

where $\text{HIST}(f, \delta x)$ represent the histogram of the function f with bins of size δx , and K is the number of channel matrix samples. In this case, histograms are computed by treating each combination of the channel matrix, the receive antenna element, and the transmit antenna element as an observation. Fig. 7(a) shows the histogram of the magnitude of the responses obtained from a typical frequency bin. The dotted line is the ideal Rayleigh distribution with $\sigma = 0.4$. As expected, the histogram of the measured magnitude is close to the Rayleigh distribution. Fig. 7(b) shows the histogram of the phases. It is observed that the measured phase of the responses is close to the uniform distribution.

D. Frequency Correlation Functions

The frequency response $H(f_i, t)$ computed from the measured samples can be interpreted as a random process [24]. Here, we evaluate the frequency correlation coefficients by averaging the channel response associated with the frequency bin over both the time and spatial domains. The autocorrelation function of this process is given by

$$\mathbf{R}(k, 0) = \frac{1}{\Omega} \sum_{i=1}^{\Omega-k} h^H(f_i, t) h(f_{i+k}, t) \quad k \geq 0 \quad (4)$$

where $h(f_i, t)$ is the complex frequency response associated with frequency bin f_i at time t , and Ω is the number of frequency bins. Fig. 8 shows the envelopes of the frequency correlation function from the measured data. The x axis is the frequency separation. The frequency correlation varies with the interelement spacing and environment. In our NLOS scenarios, the frequency correlation coefficient decays with the frequency separation. This characteristic from outdoor measurement data is similar to the results reported in [5], which were taken from indoor MIMO channel measurements. Note also that based on Fig. 8, the coherence bandwidth (frequency correlation function over 0.9) is around 50 kHz, which is wider than the aforementioned ballpark estimate. However, it is still far smaller than the signal bandwidth of 2.5 MHz.

V. MEASURED MIMO CHANNEL CAPACITY AND KRONECKER MODELING

In this section, we examine two issues based on our channel measurement data. First, we compute the wideband MIMO channel capacity from the measured data, and compare that to the

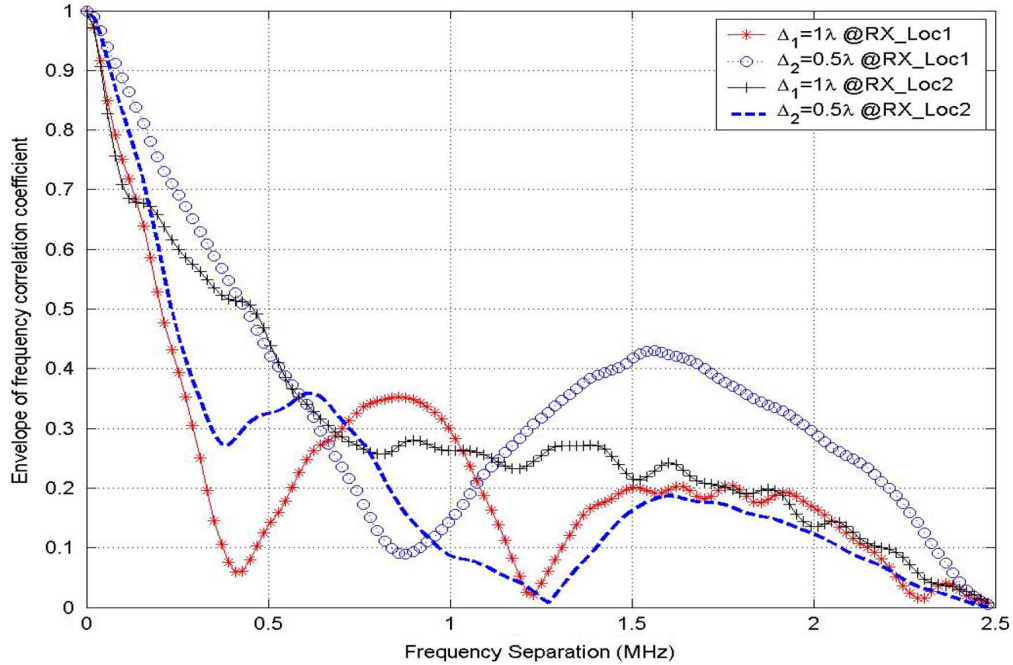


Fig. 8. The frequency correlation functions resulted from different sites and Rx interelement spacing.

narrowband case. Second, we evaluate the Kronecker channel model [5], [21] to test its validity under different array sizes.

A. Measured MIMO Channel Capacity

Based on the channel responses in a frequency bin, the capacity of a wideband MIMO channel can be calculated by dividing the frequency band (BW) of interest into Ω narrowband frequency bins, each having a bandwidth of BW/Ω Hz [22]. Assuming no knowledge of the channel state information at the Tx, the narrowband channel capacity C_{nb} is given by

$$C_{\text{nb}}(f) = \log_2 \left[\det \left(\mathbf{I}_{M_R} + \frac{\rho}{M_T} \mathbf{H}(f) \mathbf{H}^H(f) \right) \right] \quad (\text{bits/s/Hz}) \quad (5)$$

where $f = 1, 2, \dots, \Omega$ is the subchannel index, $\mathbf{H}(f) \in C^{M_R \times M_T}$ is the channel frequency responses with M_T Tx antennas and M_R Rx antennas, \mathbf{I}_{M_R} is the identity matrix of size $M_R \times M_R$, ρ represents the average SNR, and $(\bullet)^H$ denotes the Hermitian transpose of a matrix.

The wideband MIMO channel capacity C_{wb} can be expressed in terms of the narrowband capacities as follows [22]:

$$C_{\text{wb}} = \frac{1}{\Omega} \sum_{f=1}^{\Omega} C_{\text{nb}}(f). \quad (6)$$

Since the actual received signal strength varies with the Tx and Rx locations, channel normalization is necessary to facilitate a comparison of the capacities at different locations. A reasonable normalization is to scale the channel matrix such that the average power transfer between a Tx and an Rx antenna is unity

[5], [10]. Therefore, the Frobenius norm is applied to normalize $\mathbf{H}(f)$

$$\hat{\mathbf{H}}(f) = \mathbf{H}(f) \times \left[\frac{1}{\Omega M_T M_R} \sum_{f=1}^{\Omega} \|\mathbf{H}(f)\|_F^2 \right]^{-1/2} \quad (7)$$

and $\hat{\mathbf{H}}(f)$ is used in place of $\mathbf{H}(f)$ in (5).

In [25], we reported on the capacities of the 4×8 wideband channel based on our measured data and compared them with those of the ideal iid matrix channel with zero-mean complex Gaussian entries. We found that the measured capacity within the 2.5 MHz bandwidth is about 70% of that of the iid channel at RX_Loc2 and about 86% at RX_Loc1. Here, we further evaluate the capacity for different array sizes. We choose the subsets of the measured data that correspond to the array sizes 2×2 , 3×3 , and 4×4 . Fig. 9 compares the CDF of the normalized capacity (in bits/s/Hz) between the wideband channel and the narrowband channel with $\rho = 10$ dB. Observe that the mean capacity does not change significantly, but the curves for the wideband capacity become steeper than those of the narrowband. The outage capacity of the wideband channel increases over the frequency-flat case. For example, the 10% outage capacities increase from 4.7 to 5.2, 6.7 to 7.15, and 8.7 to 9.0 for the 2×2 , 3×3 , and 4×4 systems, respectively. We believe this is because the wideband result is the average capacity over all frequency bins, and thus is less sensitive to the frequency fades than the narrowband case. Our results are consistent with those reported in [6], in which the authors took the wideband indoor channel measurement by using a virtual MIMO channel sounder at 5.2 GHz.

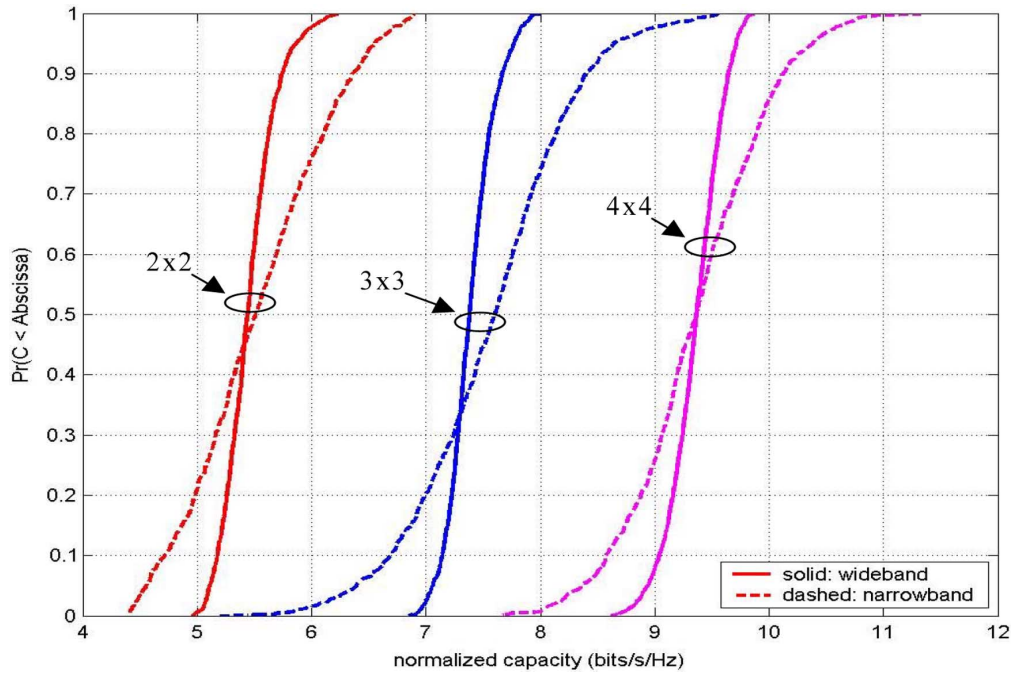


Fig. 9. Comparisons of the CDF capacity of narrowband versus wideband (which is normalized to the unit bandwidth).

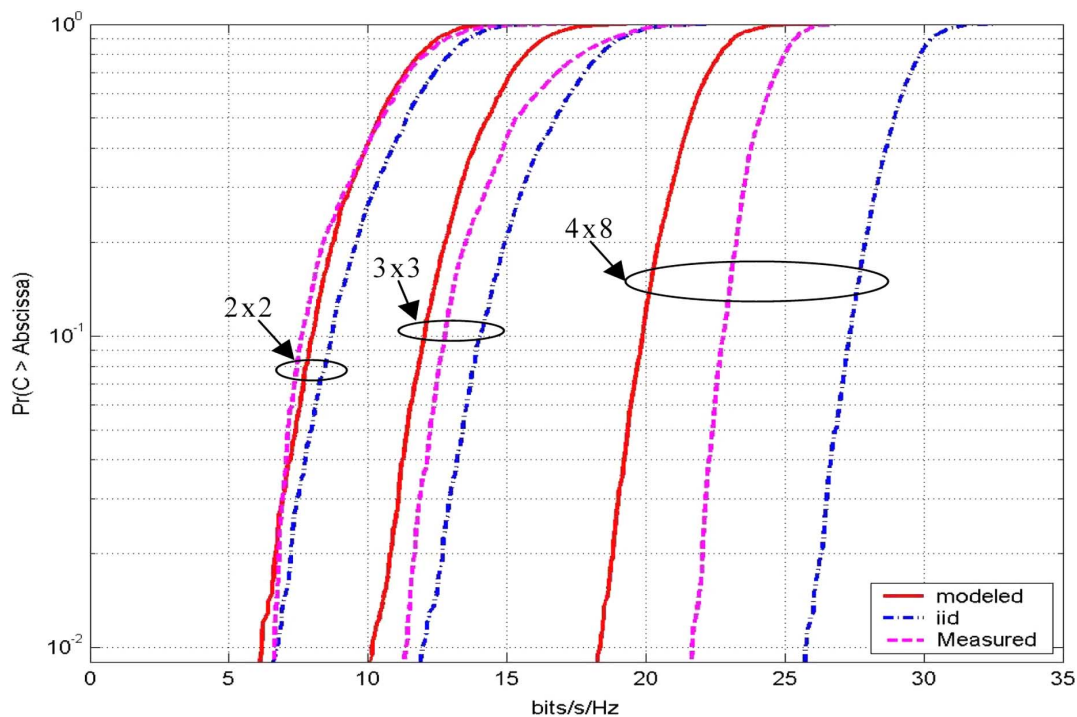


Fig. 10. CDF capacity of the Kronecker model, the measured, and the iid in subarray 2×2 , 3×3 , and 4×8 MIMO systems.

B. Evaluation of the Kronecker MIMO Channel Model

By applying the measured channel responses in a frequency bin, we can evaluate the Kronecker model [26]. Fig. 10 compares the CDF of the capacity derived from the measured data, the Kronecker model, and the iid simulation. Results from the 2×2 subarray, the 3×3 subarray, and the full 4×8 MIMO system are shown together. Observe that the Kronecker model

approximates the measured channel very well for the 2×2 subarray system. With the increase of the array size, however, the model error becomes gradually more significant in terms of the CDF capacity. Specifically, the Kronecker model may overestimate the correlation of the transmit antennas and the receive antennas in a MIMO system with larger array sizes in an outdoor environment. Our results are similar to the findings of [21], in which the authors took indoor channel measurements with a

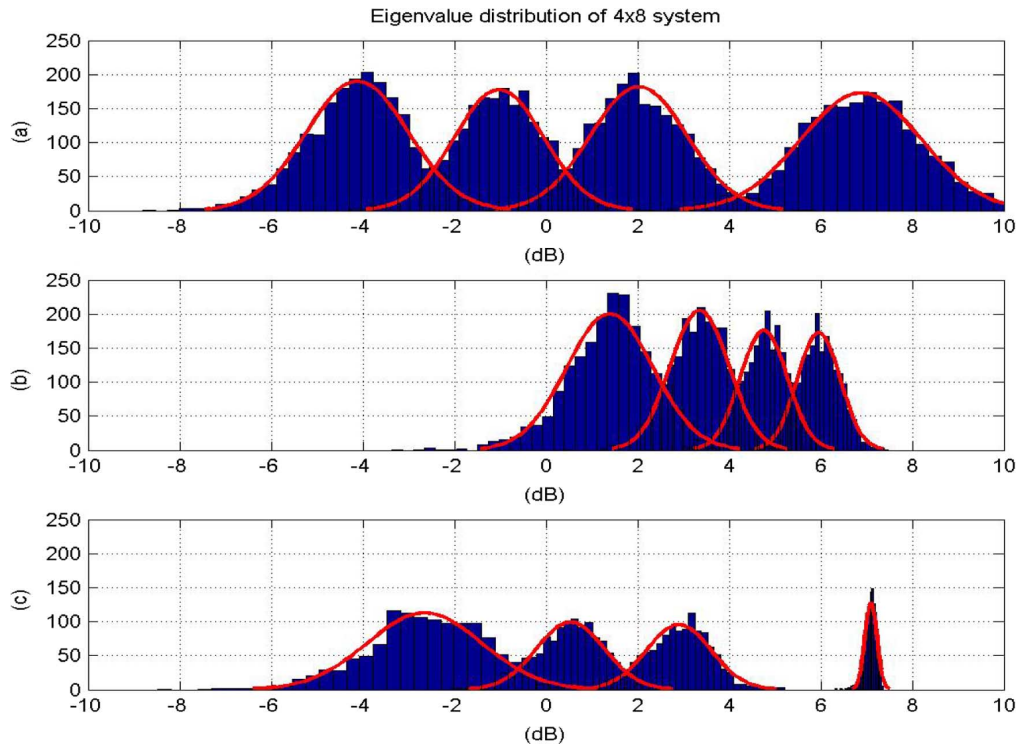


Fig. 11. Comparison of the distributions of eigenvalues from (a) the Kronecker model; (b) the iid simulation; and (c) the measured data in a 4×8 MIMO system.

virtual MIMO channel sounder at 5.2 GHz with a bandwidth of 120 MHz.

Because the distribution of the eigenvalues of $\mathbf{H}\mathbf{H}^H$ plays a key role in the MIMO channel capacity, comparisons are made of the PDF of eigenvalues from the measured channel, the Kronecker model, and the iid simulation in the 4×8 system in Fig. 11. Observe that the distributions of the four eigenvalues are quite different among the Kronecker model, the iid simulation, and the measured channel. The large spread of the eigenvalues in the Kronecker model results in lower channel capacities due to higher spatial correlation among antenna elements. This spread leads to the lower capacity CDF of the Kronecker MIMO channel model.

VI. CONCLUSION

We have presented measurement results of wideband MIMO channels in outdoor NLOS environments using a true array channel sounder. Our channel sounder consists of four transmit antennas and eight receive antennas with a bandwidth of 2.5 MHz. It is capable of capturing all 32 channel responses simultaneously through the transmission of four circularly shifted probing PN sequences at the same time. After obtaining the impulse responses of the matrix channels from the data collected in a NLOS environment, the wideband channel capacities were computed and compared with the narrowband results for the 2×2 , 3×3 , and 4×4 systems. We found that the CDF of the normalized capacity becomes steeper for wideband channels than for narrowband channels, meaning a more stable performance for a wideband MIMO system than a narrowband one. Finally, we evaluated the Kronecker model with the measured data and found that while the correlation of

the Kronecker model is similar to that of the measured data for a small number of array elements, it tends to overestimate the correlation among the antennas for arrays of larger sizes.

ACKNOWLEDGMENT

The authors appreciate Dr. W. Vogel's insights into the measurement results and the help from F. Wang, X. Yang, and J. Soric during the measurement campaigns.

REFERENCES

- [1] G. F. Foschini and M. J. Gans, "On limits of wireless communications in a fading environment when using multiple antennas," *Wireless Pers. Commun.*, vol. 6, pp. 311–335, Mar. 1998.
- [2] I. E. Telatar, *Capacity of Multiantenna Gaussian Channels*. New York: AT&T Bell Laboratories, Jun. 1995, Tech. Memo.
- [3] D. Shiu, G. J. Foschini, M. J. Gans, and J. M. Kahn, "Fading correlation and its effects on the capacity of multielement antenna systems," *IEEE Trans. Commun.*, vol. 48, pp. 502–513, Mar. 2000.
- [4] D. P. Palomar, J. R. Fonollosa, and M. A. Lagunas, "Capacity results of spatially correlated frequency-selective MIMO channels in UMTS," in *Proc. IEEE Veh. Technol. Conf.*, 2001, vol. 2, pp. 553–557.
- [5] K. Yu, M. Bengtsson, B. Ottersten, D. McNamara, P. Karlsson, and M. Beach, "Modeling of wide-band MIMO radio channels based on NLOS indoor measurements," *IEEE Trans. Veh. Technol.*, vol. 53, no. 3, pp. 655–665, 2004.
- [6] A. F. Molisch, M. Steinbauer, M. Toeltsch, E. Bonek, and R. S. Thoma, "Capacity of MIMO systems based on measured wireless channels," *IEEE J. Sel. Areas Commun.*, vol. 20, pp. 561–569, Apr. 2002.
- [7] P. C. F. Eggers, I. Z. Kovacs, K. Olesen, and G. Kuijpers, "Measurements of wideband multi-element transmit-receive diversity channels in the UMTS-band," in *Proc. IEEE 52nd Veh. Technol. Conf.*, 2000, vol. 4, pp. 1683–1689.
- [8] P. Kyritsi, P. C. F. Eggers, and A. Oprea, "Dual domain coherence measures for FWA channels in the 5–6 GHz band," in *Proc. IEEE 56th Veh. Technol. Conf.*, 2002, vol. 1, pp. 111–115.
- [9] D. Chizhik, J. Ling, P. Wolniansky, R. Valenzuela, N. Costa, and K. Huber, "Multiple-input-multiple-output measurements and modeling in Manhattan," *IEEE J. Sel. Areas Commun.*, vol. 21, no. 3, pp. 321–331, Apr. 2003.

- [10] J. W. Wallace, M. Jensen, A. L. Swindlehurst, and B. Jeffs, "Experimental characterization of the MIMO wireless channel: Data acquisition and analysis," *IEEE Trans. Wireless Commun.*, vol. 2, no. 2, pp. 335–343, 2003.
- [11] M. A. Jensen and J. W. Wallace, "A review of antennas and propagation for MIMO wireless communications," *IEEE Trans. Antennas Propag.*, vol. 52, pp. 2810–2824, Nov. 2004.
- [12] M. Bataïri, J. Kepler, T. Krauss, S. Mukthanvaram, J. Porter, and F. Vook, "An experimental OFDM system for broadband mobile communications," in *Proc. IEEE Veh. Technol. Conf.*, 2001, vol. 4, pp. 1947–1951.
- [13] D. P. McNamara, M. A. Beach, and P. N. Fletcher, "Experimental investigation of the temporal variation of MIMO channels," in *Proc. IEEE 54th Veh. Technol. Conf.*, Atlantic City, NJ, Oct. 7–11, 2001, pp. 1063–1067.
- [14] J. O. Nielsen, J. B. Andersen, P. C. F. Eggers, G. F. P. Pedersen, K. Olesen, and H. Suda, "Measurements of indoor 16×32 wideband MIMO channels at 5.8 GHz," in *Proc. IEEE 8th Int. Symp. Spread Spectrum Tech. Applicat.*, 2004, pp. 864–868.
- [15] J. B. Andersen, J. O. Nielsen, G. F. P. Pedersen, K. Olesen, P. Eggers, E. H. Sorensen, and S. Denno, "A 16 by 32 wideband multichannel sounder at 5 GHz for MIMO," in *IEEE Int. Antennas Propag. Soc. Symp. Dig.*, 2004, vol. 2, pp. 1263–1266.
- [16] W. A. T. Kotterman, G. F. Pedersen, K. Olesen, and P. Eggers, "Correlation properties for radio channels from multiple base stations to two antennas on a small handheld terminal," in *Proc. IEEE 56th Veh. Technol. Conf.*, 2002, vol. 1, pp. 462–466.
- [17] —, "Cable-less measurement set-up for wireless handheld terminals," in *Proc. 12th IEEE Int. Symp. Pers., Indoor and Mobile Radio Commun.*, 2001, vol. 1, pp. B-112–B-116.
- [18] V. Erceg, P. Soma, D. S. Baum, and S. Catreux, "Multiple-input multiple-output fixed wireless radio channel measurements and modeling using dual-polarized antennas at 2.5 GHz," *IEEE Trans. Wireless Commun.*, vol. 3, no. 6, pp. 2288–2298, Nov. 2004.
- [19] V. Erceg, P. Soma, D. S. Baum, and A. Paulraj, "Capacity obtained from multiple-input multiple-output channel measurements in fixed wireless environments at 2.5 GHz," in *Proc. IEEE Int. Conf. Commun.*, 2002, vol. 1, pp. 396–400.
- [20] D. S. Baum, D. Gore, R. Nabar, S. Panchanathan, K. V. S. Hari, V. Erceg, and A. J. Paulraj, "Measurement and characterization of broadband MIMO fixed wireless channels at 2.5 GHz," in *Proc. IEEE Int. Conf. Pers. Wireless Commun.*, 2000, pp. 203–206.
- [21] H. Ozelik, M. Herdin, W. Weichselberger, J. Wallace, and E. Bonek, "Deficiencies of 'Kronecker' MIMO radio channel model," *Electron. Lett.*, vol. 39, pp. 1209–1210, Aug. 2003.
- [22] A. Paulraj, R. Nabar, and D. Gore, *Introduction to Space-Time Wireless Communications*. Cambridge, U.K.: Cambridge Univ. Press, 2003.
- [23] T. S. Rappaport, *Wireless Communications: Principle and Practice*. Englewood Cliffs, NJ: Prentice-Hall PTR, 2002.
- [24] K. Pahlavan and A. H. Levesque, *Wireless Information Networks*. New York: Wiley, 1995.
- [25] Y. Yang, G. Xu, and H. Ling, "Wideband MIMO measurements of outdoor NLOS channels," *Microw. Opt. Technol. Lett.*, vol. 48, no. 2, pp. 216–218, Feb. 2006.
- [26] J. P. Kermaoal, L. Schumacher, K. I. Pedersen, P. E. Mogensen, and F. Frederiksen, "A stochastic MIMO radio channel model with experimental validation," *IEEE J. Sel. Areas Commun.*, vol. 20, no. 6, pp. 1211–1226, Aug. 2002.



Yaoqing Yang (M'06) received the B.S. degree from the Northern Jiantong University, Beijing, China, in 1983, and the M.S. degree from the Beijing Broadcast Institute, Beijing, in 1986, both in electrical engineering. He received the Ph.D. degree in the area of wireless communications and networks from the University of Texas at Austin in May 2006.

He served as a lecturer and engineer at the Beijing Broadcast Institute between December 1986 and July 1997. In August 1997, he was a visiting scholar with the University of Texas at Austin, where he worked on

a semiconductor project sponsored by the National Science Foundation (NSF). From 2000 to 2002, he worked on the Advanced Research Program (ARP) project for smart antenna measurements. Later, he developed a 4×8 wideband MIMO channel sounder that incorporated spread spectrum technology. In August 2006, he joined the faculty of the Department of Computer and Electronics Engineering, University of Nebraska-Lincoln (Omaha Campus). His current research interests lie in wireless communication systems with emphasis on MIMO channel characterization, array signal processing, and RF engineering.



Guangan Xu (M'91) received the Ph.D. degree in electrical engineering from Stanford University, Stanford, CA, in 1991.

During summer 1989, he was a Research Fellow with the Institute of Robotics, Swiss Institute of Technology, Zurich, Switzerland. From 1990 to 1991, he was a General Electric fellow of the Fellow-Mentor-Advisor Program, Center of Integrated Systems, Stanford University. From 1991 to 1992, he was a Research Associate with the Department of Electrical Engineering, Stanford University,

and a short-term visiting scientist with the Laboratory of Information and Decision Systems, Massachusetts Institute of Technology (MIT), Cambridge. In 1992, he joined the Department of Electrical and Computer Engineering, The University of Texas at Austin, and was later promoted to Tenured Associate Professor. He cofounded Navini Networks based in Richardson, TX, in September 2000, where he was also Chief Technical Officer. In November 2004, he returned to China and was a Chief Scientist of Beijing Xinwei Telecom Technology, Inc., which he cofounded in 1995.

Dr. Xu is the recipient of 1995 NSF CAREER Award and the 1996 IEEE TRANSACTIONS ON SIGNAL PROCESSING Young Author Best Paper Award. He was the original author of the ITU Third-Generation (3G) (TD-SCDMA) Standard and the recipient of the First Class Award of 2001 Science and Technology Advancement from Chinese government. He was also awarded "Asian Engineer of the Year" by Chinese Institute of Engineers in 2003.



Hao Ling (S'83–M'86–SM'92–F'99) was born in Taichung, Taiwan, on September 26, 1959. He received the B.S. degrees in electrical engineering and physics from the Massachusetts Institute of Technology (MIT), Cambridge, in 1982, and the M.S. and Ph.D. degrees in electrical engineering from the University of Illinois at Urbana-Champaign, in 1983 and 1986, respectively.

He joined the faculty of the University of Texas at Austin in September 1986 and is currently Professor of Electrical and Computer Engineering and holds the L. B. Meaders Professorship in Engineering. During 1982, he was with the IBM Thomas J. Watson Research Center, Yorktown Heights, NY, where he conducted low-temperature experiments with the Josephson Department. He participated in the Summer Visiting Faculty Program in 1987 at the Lawrence Livermore National Laboratory, Livermore, CA. In 1990, he was an Air Force Summer Fellow with Rome Air Development Center, Hanscom Air Force Base, MA. His principal area of research is in computational electromagnetics. During the past two decades, he has actively contributed to the development and validation of numerical and asymptotic methods for characterizing the radar cross section from complex targets. His recent research interests also include radar signal processing, antenna design and propagation channel modeling.

Dr. Ling was a recipient of the National Science Foundation Presidential Young Investigator Award in 1987, the NASA Certificate of Appreciation in 1991, as well as several teaching awards from the University of Texas.